



# Suspension High Velocity Oxy-Fuel (SHVOF)-Sprayed Alumina Coatings: Microstructure, Nanoindentation and Wear

J. W. Murray, A. S. M. Ang, Z. Pala, E. C. Shaw, and T. Hussain

(Submitted August 8, 2016; in revised form September 19, 2016)

Suspension high velocity oxy-fuel spraying can be used to produce thermally sprayed coatings from powdered feedstocks too small to be processed by mechanical feeders, allowing formation of nanostructured coatings with improved density and mechanical properties. Here, alumina coatings were produced from submicron-sized feedstock in aqueous suspension, using two flame combustion parameters yielding contrasting microstructures. Both coatings were tested in dry sliding wear conditions with an alumina counterbody. The coating processed with high combustion power of 101 kW contained 74 wt.% amorphous phase and 26 wt.% crystalline phase (95 wt.% gamma and 3 wt.% alpha alumina), while the 72-kW coating contained lower 58 wt.% amorphous phase and 42 wt.% crystalline phases (73 wt.% was alpha and 26 wt.% gamma). The 101-kW coating had a dry sliding specific wear rate between 4 and  $4.5 \times 10^{-5} \text{ mm}^3/\text{Nm}$ , 2 orders of magnitude higher than the 72-kW coating wear rate of  $2\text{--}4.2 \times 10^{-7} \text{ mm}^3/\text{Nm}$ . A severe wear regime dominated by brittle fracture and grain pullout of the coating was responsible for the wear of the 101-kW coating, explained by mean fracture toughness three times lower than the 72-kW coating, owing to the almost complete absence of alpha alumina.

**Keywords** alpha alumina, dry sliding wear, gamma alumina, HVFSFS, Rietveld refinement, SHVOF

## 1. Introduction

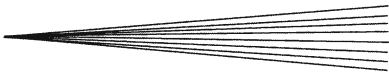
High velocity oxy-fuel (HVOF) spraying is a useful method of depositing a range of material types, including metals, ceramics, and cermets, onto substrates. The suspension variant of the process—SHVOF, also known as high velocity suspension flame spraying (HVFSFS), allows micron- and submicron-sized particles to be directly fed into the combustion flame and results in a more dense coating compared to conventional HVOF. Such powders are difficult to process with mechanical powder feeders, due to a high likelihood of agglomeration, and hence reduced flowability (Ref 1). Health risks involved with use of submicron particles are also somewhat mitigated. There is also an increased likelihood of preserving the original crystalline phase (Ref 2) because part of the input thermal energy is used for evaporation of the liquid, as opposed to it transferring to the particles themselves (Ref 3). Since the coating microstructures reflect the feedstock material, thin as well as thick coatings can be developed, typically

exhibiting fine microstructures and hence can exhibit superior mechanical properties.

Alumina is an engineering ceramic often used as a feedstock for thermally sprayed coatings, owing to its low cost as well as high hardness, good wear resistance and chemical stability (Ref 4). In its sintered form, alumina is normally comprised of the stable alpha phase (corundum) which exhibits the best mechanical and tribological properties among the alumina phase types. Upon flame or plasma spraying, the metastable gamma form of alumina is expected to nucleate from the molten splats given its lower free critical energy for nucleation (Ref 5), while the cooling rate of such processes is often rapid enough [ $10^6\text{--}10^9 \text{ K/s}$  (Ref 6)] to avoid transformation to the delta or alpha forms (Ref 7). However, under plasma spraying for example, some amounts of delta and theta alumina have been detected along with gamma alumina (Ref 8, 9). Given the tendency for alumina to transform from the alpha phase, SHVOF spraying is a potentially useful method of preserving the alpha alumina phase in a thermally sprayed coating, via the use of a micron/submicron-sized feedstock.

Bolelli et al. (Ref 4) showed that a dense SHVOF alumina coating yielded the lowest alpha/gamma ratio compared to regular HVOF and atmospheric plasma spraying, due to more extensive melting of the feedstock powder and almost complete avoidance of the alpha phase. Toma et al. (Ref 10) produced alumina coatings using SHVOF, in which the coating was comprised of a majority (60 wt.%) alpha alumina phase with remainder gamma, in contrast to a majority gamma phase coating with a minority of alpha (30 wt.%) produced using standard HVOF. It, however, must be noted that processing

J.W. Murray, Z. Pala, E.C. Shaw, and T. Hussain, Faculty of Engineering, University of Nottingham, Nottingham NG7 2RD, UK; and A.S.M. Ang, Faculty of Science, Engineering and Technology, Swinburne University of Technology, Melbourne, VIC 3122, Australia. Contact e-mail: tanvir.hussain@nottingham.ac.uk.



conditions were not the same for both tests and hence it is difficult to make a direct comparison. Importantly, it indicates that the retention of a large amount of alpha alumina and avoidance of the gamma phase is possible, when the SHVOF spray parameters are not too severe (Ref 4, 11). Tribological testing of SHVOF in comparison with regular HVOF-sprayed alumina coatings has been performed by Rauch et al. (Ref 11), with an order of magnitude reduction in wear rate for the SHVOF coating containing ~3 wt.% alpha alumina. However, a much smaller reduction in wear rate was seen for the coating containing a much larger (~33 wt.%) amount of alpha alumina. This finding is in contrast to the expected tribological benefit from a high level of alpha alumina present in a thermally sprayed coating. Hence, based on the current literature regarding SHVOF alumina coatings, it is not clear which parameters result in an alpha-rich coating, nor is it understood what influence submicron scale crystalline alumina distributed within the coating has on the tribological properties. The aim of this work is therefore to produce two alumina coating types using SHVOF with different levels of alpha alumina and to evaluate dry sliding wear performance with reference to fundamental material properties.

By varying the SHVOF combustion flame power, a range of coatings with various levels of porosity and microstructure was produced and the two parameters in this paper were deliberately selected at the extreme ends of the initially large range of parameters investigated prior to this work, containing very different levels of porosity, and alpha and gamma alumina. Dry sliding wear testing was performed on the two selected coating types, and location-specific nanoindentation was carried out on coating cross-sections to quantify the mechanical properties of phases present and hence explain the tribological behavior of SHVOF alumina coatings and its dependence on alumina phase type. Fracture toughness measurement was also conducted via microhardness indentation and crack length examination. Rietveld analysis was conducted on the x-ray diffraction data to quantify the crystalline and amorphous phases present.

## 2. Experimental

### 2.1 Materials and Suspension Spraying

The suspension feedstock was prepared using corundum (100% alpha alumina) powder CR1 (Baikowski, France) with a D50 particle size of 1  $\mu\text{m}$  in a suspension of deionized water at a concentration of 35 wt.%, which was mechanically stirred for 2 h before spraying. No dispersant was used in the alumina suspension; however, pH was balanced in such a way that the zeta potential fell within the stable range. The SHVOF coating was deposited onto carbon steel substrates with dimensions of 60  $\times$  25  $\times$  2 mm. All substrates were grit blasted and cleaned with alcohol before coating. A modified UTP TopGun HVOF spray system, with a 0.3-mm suspension injector diameter was used for spraying. Hydrogen fuel

was combusted in a 22-mm-long chamber, into which the suspension was fed at a pressure of 3 bar from a mechanically stirred, pressurized chamber. Injection flow rate was 100 mL/min for all tests. Substrates were mounted on a rotating carousel at 73 rpm (substrate speed of 1 m/s), while the spray gun was traversed perpendicular to the substrate movement direction, at a speed of 5 mm/s, resulting in an inter-pass step of 4 mm, until a coating thickness of approximately 60  $\mu\text{m}$  was achieved. Spray parameters are shown in Table 1. The standoff distance was fixed at 85 mm for both coatings.

### 2.2 Coating Characterization

Cross-sections of samples were cut using a precision silicon carbide circular saw and were polished using 1- $\mu\text{m}$  diamond grit prior to inspection. Microscopy imaging (SEM) was carried out using an FEI XL30 SEM in backscattered electron (BSE) mode for cross-sections and secondary electron (SE) mode for surface inspection. X-ray diffraction (XRD) was performed with a Bruker D5000 equipped with point detector and using Cu  $K\alpha$  radiation, wavelength 0.154 nm, and scanning from 5 to 120°  $2\theta$  values, with a step size of 0.04°  $2\theta$  and a step time of 24 s. Rietveld refinement (Ref 12) of XRD data was performed in TOPAS (Bruker) software package for determination of alpha and gamma alumina quantities as well as estimation of the degree of crystallinity. Since the amorphous phase is displayed as two broad halos, or humps, in diffraction patterns, two pseudo-Voigt profiles were used for its fitting. Similarly to Ref 13, the background was fitted by a Chebyshev polynomial of the first kind with only one coefficient being refined during the Rietveld refinement procedure. The degree of crystallinity (DoC) was computed as the ratio of total integral intensity of fitted crystalline reflections to the sum of crystalline and amorphous areas. No calibration was used, due to the same chemical composition of crystalline and amorphous phases, i.e., aluminum and oxygen. Crystallography information of gamma alumina was taken as a defect spinel structure from Zhou and Snyder (Ref 14).

### 2.3 Wear Testing, Nanoindentation and Fracture Toughness

Ball-on-flat dry sliding wear testing was performed with a CETR UMT-2 microtribometer (CETR, USA), using a 6.3-mm-diameter alpha alumina ball (Dejay Ltd UK) in the central regions of the coatings, after sequential polishing to a final stage of 1  $\mu\text{m}$  grit. The counterbody material was selected based on widespread applications of alumina in like-on-like wear conditions such as bearings. A load of 10 N, stroke length of 5 mm and sliding speed of 10 mm/s were used. In a previous publication, it was reported that the above loading conditions can produce suitable wear tracks in bulk alumina (Ref 17). Wear tracks were measured using a Talysurf Form 50 contact profilometer (Taylor-Hobson, UK), with a lateral resolution of 0.5  $\mu\text{m}$ . Five profiles at spacings of 1 mm were taken from the wear tracks, and the areas of the wear profiles were calculated below the mean line of the surface, and

**Table 1** Spray parameters

Sample	O <sub>2</sub> flow rate, L/min	H <sub>2</sub> flow rate, L/min	Stoichiometry, %	Standoff distance, mm	Flame power, kW
1	306	611	100	85	101
2	219	437	100	85	72

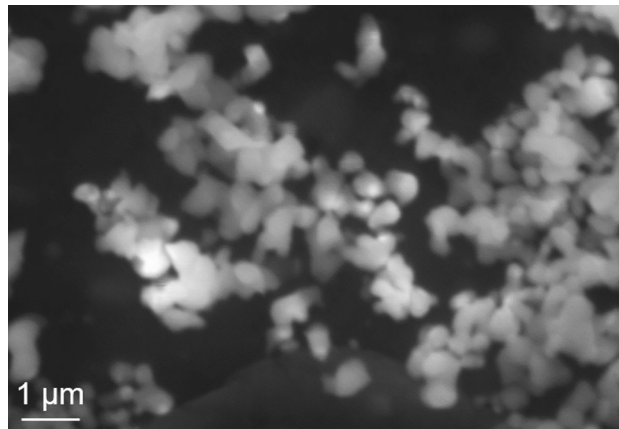
multiplied by the track length to yield volume loss. Ball wear rates were measured by taking the average diameter and converting to volume removed based on the equation for volume of a sphere. Two wear tests for each sample were performed under identical conditions to establish the repeatability of the test results.

Nanoindentation of coating cross-sections was performed using an instrumented indentation platform (Hysitron TI Premier Ti, Hysitron Inc., Minneapolis, MN), which is able to record simultaneously the applied load, and penetration depth curve for the complete loading and unloading cycle. A diamond Berkovich tip was used, and the applied load of 2500  $\mu\text{N}$  was found to be suitable to generate an indent impression with onset plastic deformation. Prior to indenting the samples, a scanning probe microscope (Hysitron in situ SPM, Hysitron Inc., Minneapolis, MN) was used to generate an image to aid the choice of indent locations for measuring the individual phases of the coating. The SPM setup consists of the same Berkovich tip used for indentation and was mounted on a high-precision 3 axis piezo scanner. A constant imaging force of 2-3  $\mu\text{N}$  was used to raster scan the probe over the sample surface at a rate of 0.2 Hz to generate the high contrast images. Post-indent SPM imaging was also done to ensure that the accuracy of the individual indent impression was within the region of interest and that no cracking had developed. A minimum of 20 indents was carried out. Hardness was measured by dividing the maximum load produced on the load-displacement curve by the area of the indent. Oliver and Pharr's method (Ref 15) was used to calculate the elastic modulus of the individual phases using the slope of the unloading curve from the same load-displacement graph.

In addition, Vickers microindentation on the coating was also performed using a load of 10 gf; other larger indent loads were found to be unsuitable because of extensive cracking around the indent. Fracture toughness was measured using Vickers microindentation with 200 gf on coating cross-sections and measuring crack lengths from the corners of the indent. The following equation was used from Evans and Charles to calculate fracture toughness (Ref 16):

$$K_{IC} = 0.16 (c/a)^{-1.5} (Ha^{1/2})$$

where  $K_{IC}$  is fracture toughness in  $\text{MPa m}^{1/2}$ ,  $c$  is average length of cracks from tips of the Vickers indent ( $\mu\text{m}$ ),  $a$  is the half average length of the diagonal of the Vickers indent ( $\mu\text{m}$ ), and  $H$  is Vickers hardness (MPa). Box plots of both hardness and toughness are used to represent the data, in which the small box is the mean, the middle line is the median value, the top and bottom of the large box are the upper and lower quartiles, respectively, the whiskers

**Fig. 1** SE image of powder feedstock

are the 99% values, and the small crosses are the maximum and minimum values.

### 3. Results

#### 3.1 Phase Identification and Coating Morphology

XRD phase analysis of the powder feedstock showed that it was pure alpha alumina. An SE image of the powder feedstock can be seen in Fig. 1. Many particles seen in the image are below 1  $\mu\text{m}$  diameter; however, this is consistent with D20 and D50 particle sizes of 0.7 and 1  $\mu\text{m}$ , respectively. It is also likely that smaller particles have agglomerated around larger ones, hence appearing more visible.

The XRD patterns of the as-sprayed coatings are shown in Fig. 2 together with the obtained Rietveld refinement results. In both coatings, the amorphous phase was calculated to dominate in weight %—with 42% crystallinity for the 72-kW sample, and only 26% at 101 kW. The amorphous phase is represented in the XRD patterns by two amorphous humps, the locations of which are shown by the blue lines in Fig. 2(b). Of the crystalline regions of the coatings, the 101-kW sample was dominated by gamma alumina (~95%) and a small level (~3%) of alpha alumina. 1-2% was attributed to alpha Fe, which results from a small level of x-ray penetration into the bulk. For the 72-kW coating, a majority of the crystalline material (~73%) was identified as alpha alumina, with ~26% fitting with gamma alumina. Again, a small percentage (<1%) could be attributed to alpha Fe.

Figure 3(c-f) presents BSE images of the two coating cross-sections. Both coatings are well bonded to the sub-

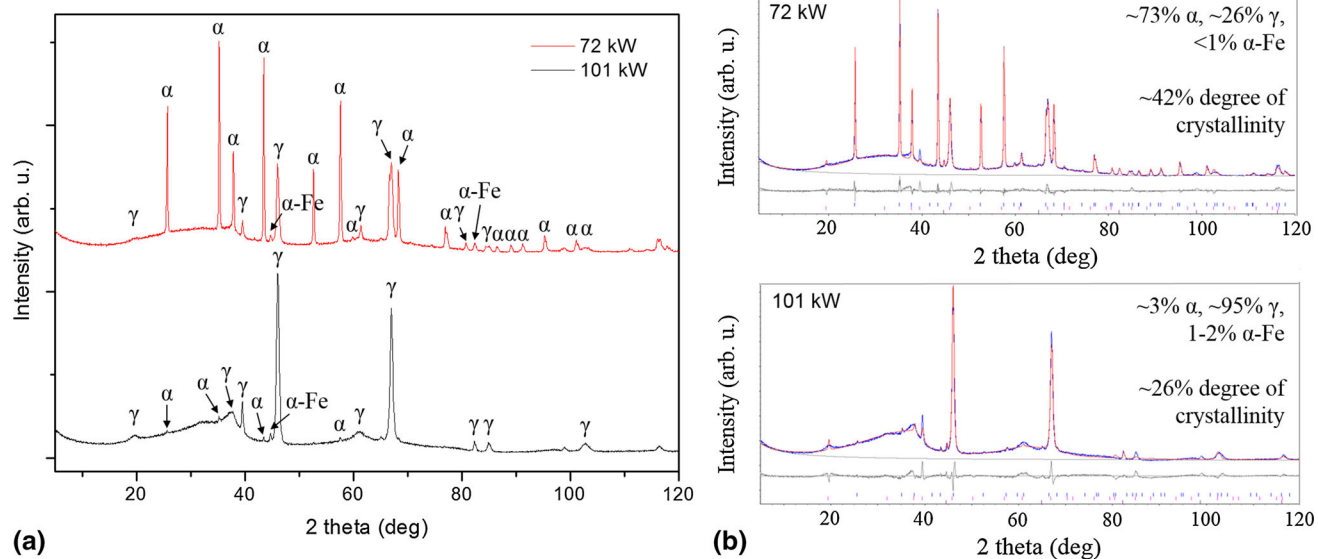


**Fig. 2** (a) XRD patterns of coatings processed with 101- and 72-kW flame energies together with (b) Rietveld refinement results showing measured data in blue, fit in red; background is the smooth line at 0 intensity; difference between data and fit plotted beneath in the form of a difference curve (Color figure online)

strate with no evidence of delamination at the coating-substrate interface. The similar thickness of both coatings (60  $\mu\text{m}$ ) is also indicative of similar deposition efficiencies, for both parameters. Vertical cracking is also present in both coatings, along with some porosity, which is less prevalent in the 101-kW sample, but is present in interlamellar bands which match the thickness of a single pass (15  $\mu\text{m}$ ). For the 72-kW coating, however, porosity is significantly more common and appears unrelated to pass geometry. In Fig. 3(e, f), three main coating features are observed, which co-relates with their individual phase. Firstly, round, light gray particles are unmelted alpha alumina fed directly from the feedstock. Light gray and splat-like structures are most likely the gamma alumina. Finally, the dark gray phase corresponds to the presence of amorphous alumina.

### 3.2 Wear Testing

Figure 4(a) presents specific wear rates for the coating wear tracks and counterbody wear scars for both coating types, and Fig. 4(b) presents coefficient of friction graphs for all wear tests.

The 72-kW processed coating exhibited specific wear rates two orders of magnitude lower than the 101-kW sample, between  $2.0$  and  $4.2 \times 10^{-7} \text{ mm}^3/\text{Nm}$  for the 72-kW and between  $4.2$  and  $4.4 \times 10^{-5} \text{ mm}^3/\text{Nm}$  for the 101-kW coatings. Counterbody wear rates also reflected this trend, with a specific wear rate of  $8.5 \times 10^{-8}$  for the 72-kW coating, compared to  $8.5 \times 10^{-6}$  for the 101-kW coating, which is 5 times lower than those of the respective coatings. Through the wear test time, the 72-kW tests underwent a gradual increase in coefficient of friction (COF) from 0.4 to over 0.45, whereas the COF for the 101-kW samples initially spiked to 0.7 before quickly

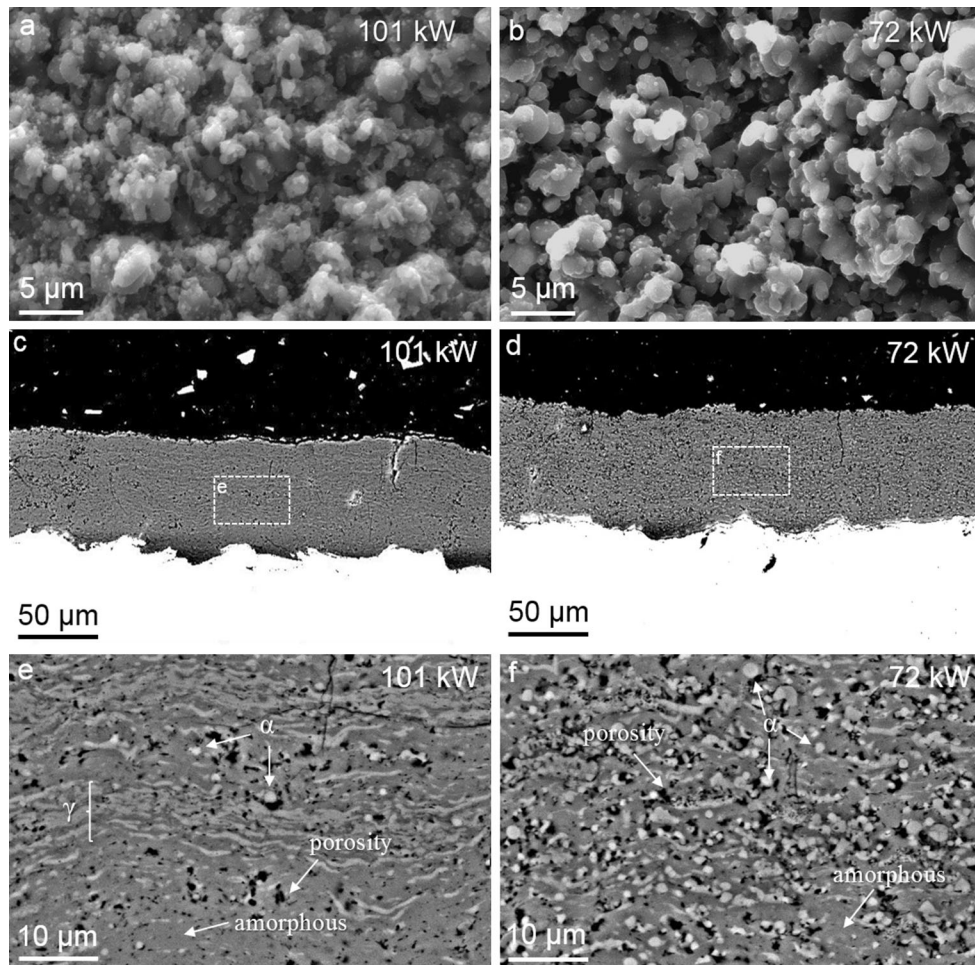
decreasing to 0.5, and then gradually lowered at a rate similar to the 72-kW coating from 0.5 to just below 0.45. The repeat test for the 101-kW coating yielded almost identical results in terms of both coating and ball wear, with the data differing by less than 5%. For the 72-kW coating, however, the second test yielded approximately half the wear rate of the first test, although measurements of such shallow tracks were challenging. The ball wear rate in the second test was 30% lower than in the first test.

Figure 5(a-c) show tilted SE images of the wear tracks on one of each of the two samples. In Fig. 5(d), line profiles across the tracks are shown. The 101-kW processed coating yielded a  $\sim 25\text{-}\mu\text{m}$ -deep wear scar with a sharp track bottom. This can be contrasted with the  $1\text{-}\mu\text{m}$ -deep round track produced in the case of the 72-kW sample. The strongly worn 101-kW sample exhibits a mostly fractured wear track characteristic of grain pullout with some plastically deformed grooves. The shallow 72-kW wear track, however, is entirely smooth without signs of fracture.

Figure 6 shows wear tracks for the counterbodies worn against the two coating types. The 101-kW ball shows a large wear track characterized by abrasive grooves with regions of dark wear debris. In contrast, the track of the ball worn on the 72-kW coating has a much smaller area, with no evidence of attached material.

### 3.3 Nanoindentation

To determine the hardness and elastic modulus of the distinct phases in each coating, nanoindentation was performed on coating cross-sections. Equations are taken from Oliver and Pharr's work (Ref 15). The apparent elastic modulus of the indenter specimen system (also known as reduced modulus,  $E^*$ ) can be defined as:



**Fig. 3** (a) and (b) SE images of coating morphologies, (c) and (d) low magnification, and (e) and (f) high magnification BSE images of coating cross-sections (Ref 18)

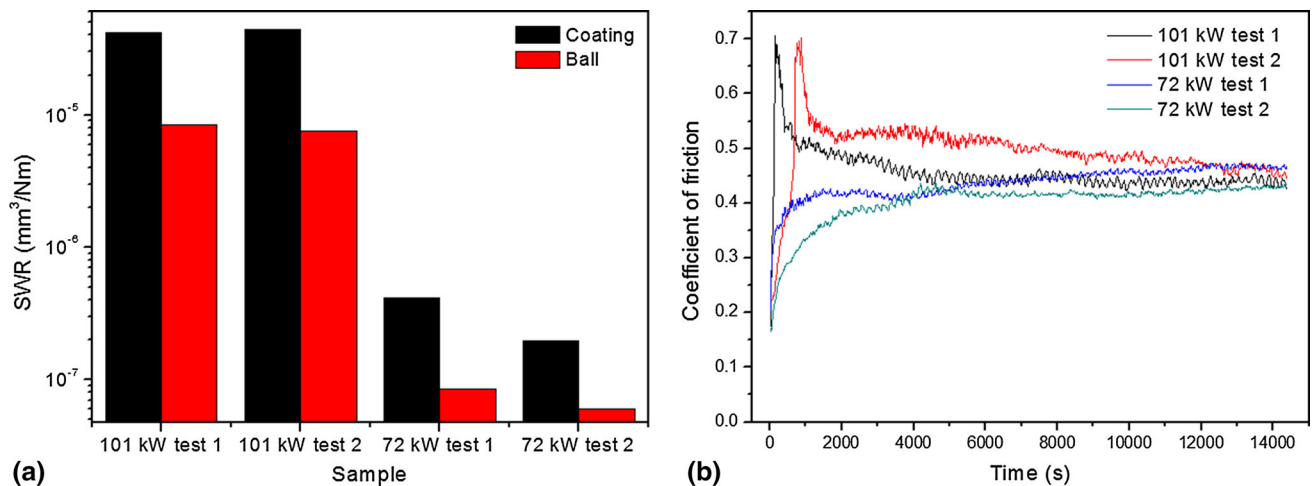


**Fig. 4** (a) Specific wear rates under dry sliding wear for the two coating types. Counterbody wear rates are also shown. (b) Coefficient of friction against wear test time for the two coatings

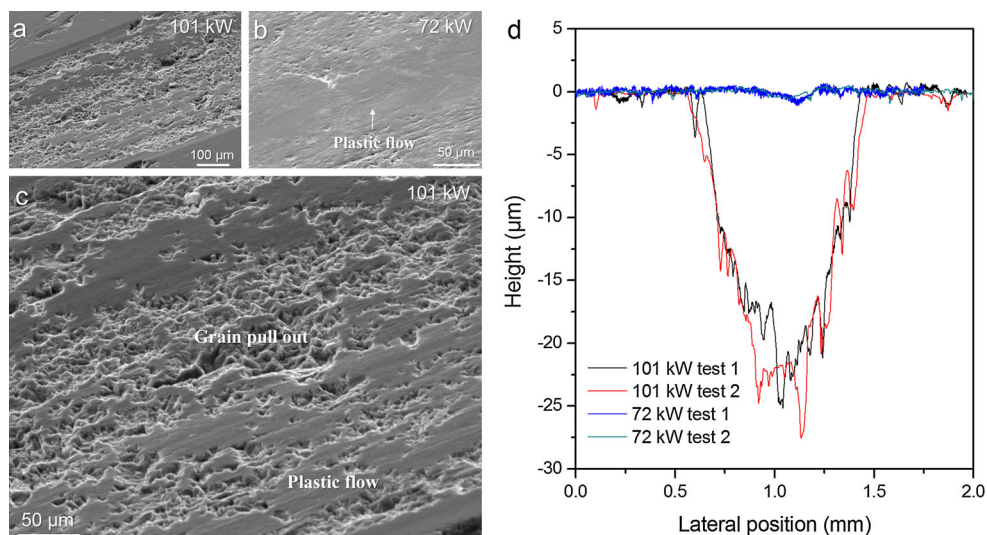


**Fig. 5** (a, b) Tilted SE images of wear tracks for both coating types, (c) high magnification image of 101-kW worn track, (d) profiles of wear tracks

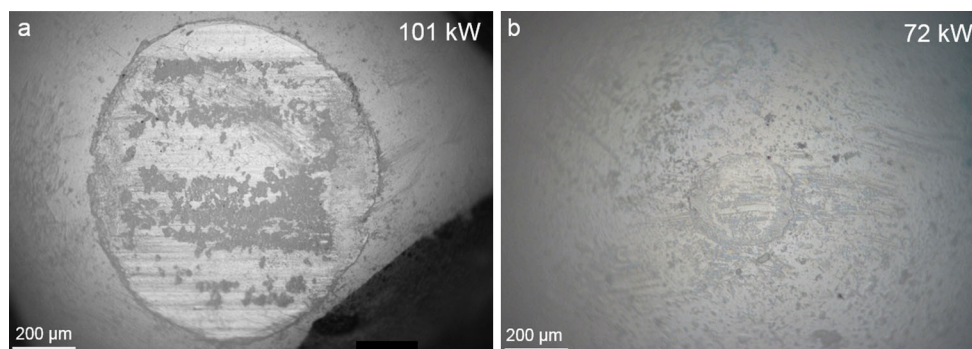


**Fig. 6** Wear tracks on alumina counterbody for (a) 101 kW and (b) 72 kW

$$E^* = \frac{1}{c^* \sqrt{A}} \left( \frac{dP}{dh_i} \right)$$

where  $A$  is the contact area of the indenter,  $dP/dh_i$  is the slope of the load/displacement curve at the initial stage of unloading, from an applied load,  $P_{\max}$ . A constant  $c^* = 1.167$  for the Berkovich tip was used. Subsequently, the elastic modulus of the coating phases was determined by accounting for the elastic effects of the non-rigid indenter. Mathematically;

$$\frac{1}{E^*} = \frac{(1 - \nu^2)}{E} + \frac{(1 - \nu_{in}^2)}{E_{in}}$$

The characteristic material properties of the diamond indenter were  $E_{in} = 1141$  GPa and  $\nu_{in} = 0.07$ , while the Poisson's ratio values for this current work were assumed to be  $\nu = 0.2$ .

The mean nanohardness and elastic modulus of the white phase and darker matrix seen in the SPM images are shown in Table 2, while the locations of the indents are shown in Fig. 7. For the purposes of these indentation

tests, phases appearing as white, which include both gamma and alpha to different amounts depending on coating type, are labeled as such, but cannot be further defined as alpha and gamma with any certainty. One can hypothesize that the round white features in SPM images are unmelted alpha particles from the feedstock. Figure 8 presents all hardness values measured in matrix and white phase regions in box plot format to demonstrate the distribution of values.

Mean matrix hardness was measured at  $9.1 \pm 3.3$  GPa in the case of the 72-kW coating. The rounded white phase, most likely to be alpha alumina particles, had a mean hardness of  $20.3 \pm 5.9$  GPa. However, absolute hardness of the phase is likely to be higher, for example as demonstrated in one indent in Fig. 7(d). Given the small size of phases measured, the surrounding matrix may contribute to the deformation during indentation and hence reducing the measured hardness. It is also noted that some indents measured in the 72-kW white phase regions are also likely to contain some gamma alumina (appearing as flattened lamellae in SPM images), the presence of which has been elucidated in earlier XRD

analysis. Average hardness of the white phase in the 101-kW coating was  $17.5 \pm 4.4$  GPa, with a matrix hardness slightly higher on average than that of the 72-kW sample at  $11.2 \pm 1.9$  GPa.

### 3.4 Microhardness and Fracture Toughness

Vickers microhardness testing is a common method used to evaluate a thermally sprayed coating's mechanical

**Table 2 Nanohardness and elastic modulus of dark matrix and white phases in both coatings**

	<i>H</i> , GPa	<i>E</i> , GPa
101 kW		
White	$17.5 \pm 4.4$	$242 \pm 34$
Dark	$11.2 \pm 1.9$	$178 \pm 26$
72 kW		
White	$20.3 \pm 5.9$	$237 \pm 44$
Dark	$9.1 \pm 3.3$	$155 \pm 42$

performance under compression loads. It was found that the 101-kW sample had a higher hardness value of  $13.1 \pm 1.0$  GPa (10 gf,  $n=11$ ) compared to the 72-kW sample of  $11.7 \pm 1.9$  GPa (10 gf,  $n=11$ ). Using the Oliver-Pharr method on the microindentation load-displacement curves, the corresponding measured elastic modulus of both SHVOF coatings are  $E_{101kW}=172 \pm 12$  GPa and  $E_{72kW}=133 \pm 14$  GPa; the 101-kW sample is harder and stiffer. Box plots of hardness values are shown in Fig. 9.

Subsequently, Vickers microindentation was performed on coating cross-sections, using a load of 200 gf sufficient to cause fracture of the coating. Seven indents were performed on each coating. In all cases, only horizontal cracking took place, and so a maximum of 2 crack lengths were measured for each indent. The 101-kW yielded  $K_{IC}$  values of a mean of  $1 \text{ MPa m}^{1/2}$ , with a relatively small range of between 0.5 and 2. The 72-kW coating yielded values between 1 and  $5.5 \text{ MPa m}^{1/2}$ , with a mean of 3.5. The results of fracture toughness calculations are shown in Fig. 10.

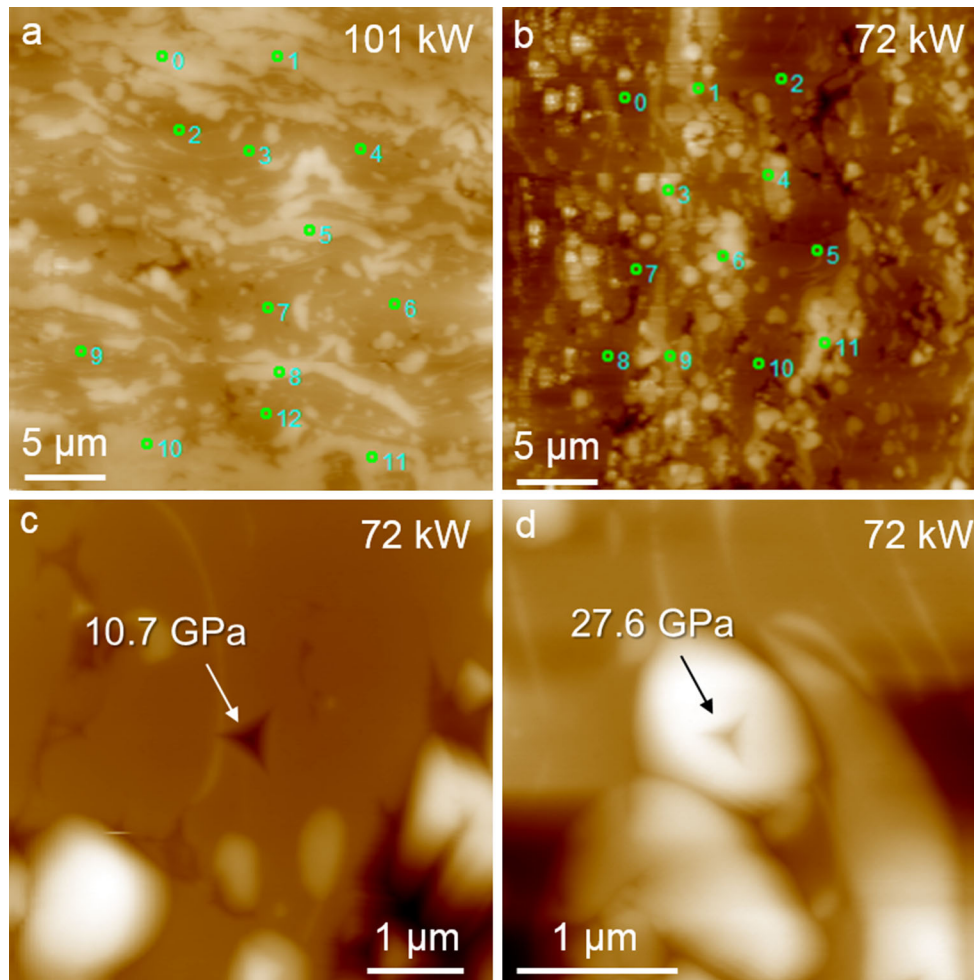


**Fig. 7** SPM images of locations of nanoindents on polished cross-sections of SHVOF samples (a) 101 kW and (b) 72 kW. (c) and (d) High magnification SPM images of individual indents

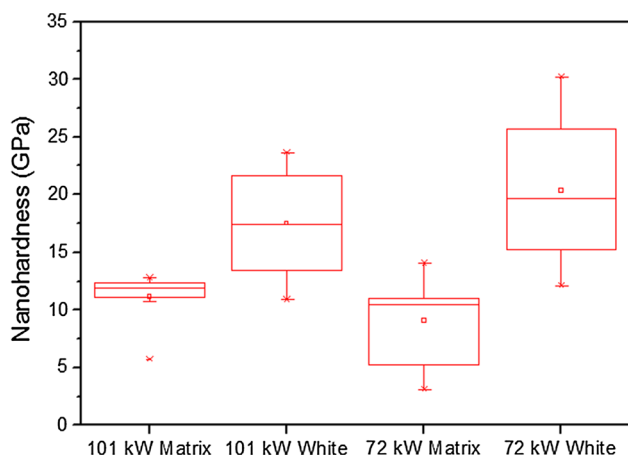


**Fig. 8** Box plots of nanohardness values for matrix and white phases present in both coatings

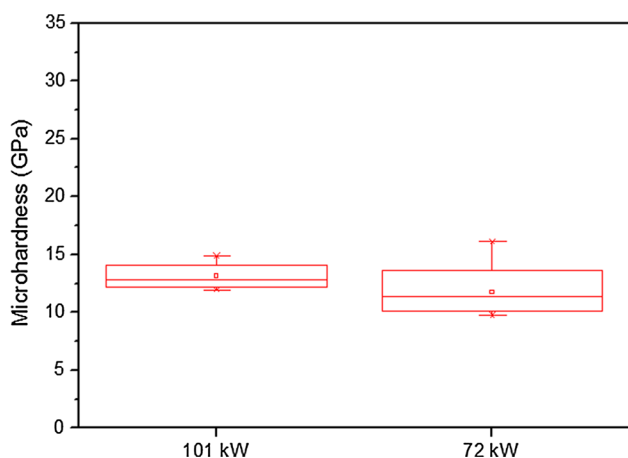


**Fig. 9** Box plots of microhardness data from the two coating cross-sections

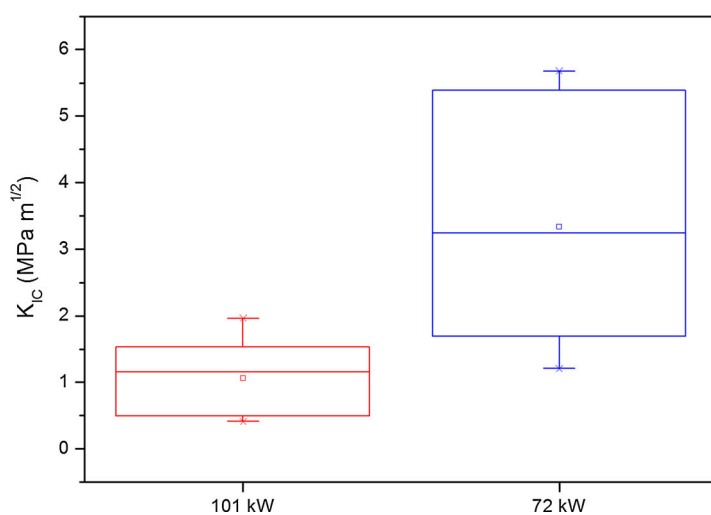
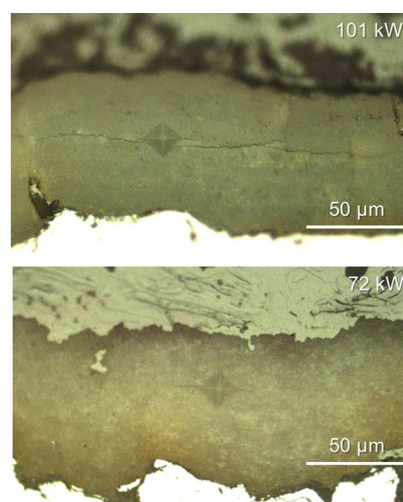


**Fig. 10** Box plots of fracture toughness and typical indents of each coating showing disparity in crack lengths

## 4. Discussion

This work has shown that a thermally sprayed alumina coating with a crystalline component dominated by the desirable alpha phase (~73 wt.% content) can be deposited using suspension HVOF with a 72-kW flame power. A 73 wt.% alpha alumina level is higher than previously obtained by Toma et al. (Ref 10). However, based on Rietveld refinement of the XRD pattern, the majority of the coating based on weight % is amorphous for both coatings types, albeit slightly lower for 72-kW coating (58 wt.% as opposed to 74 wt.% for the 101-kW coating). Using a higher flame power of 101 kW permitted almost complete melting of the feedstock material and nucleation of the metastable gamma form of alumina. Therefore, the SHVOF process does not inherently promote full coating melting and phase transformation, as was indicated by the work of Bolleli et al. (Ref 4), but the preservation of the alpha phase is dependent on the careful selection of spray parameters. It is evident that the use of the higher combustion flame power, as in the 101 kW, yielded a denser coating, with the lower degree of porosity being only present in regions matching the inter-pass spacing. Porosity in the 72-kW coating, however, appeared more uniform throughout the coating cross-section. A higher degree of porosity is consistent with a lower level of particle melting along with retention of the alpha phase. Despite some conflicting literature regarding whether the amorphous phase is present in thermally sprayed alumina coatings, the comparison here presented in the XRD results in Fig. 2 and microstructures in Fig. 3 clearly documents that consideration of only alpha and gamma alumina cannot fully describe the correct composition of the coatings. Moreover, the positions of the two amorphous humps in the XRD patterns being close to those reported in amorphous alumina (Ref 19) strengthen this argument. For comparison of morphology/porosity to





a non-suspension-based thermally sprayed alumina coating, the work of Bolelli et al. (Ref 23) can be referred to.

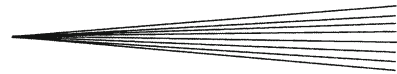
The 72-kW coating exhibited superior wear performance among the two coatings, with yielded specific wear rates separated by two order of magnitude ( $4.44 \times 10^{-5} \text{ mm}^3/\text{Nm}$  for the 101-kW coating compared to  $2.42 \times 10^{-7} \text{ mm}^3/\text{Nm}$  in the case of the 72-kW coating). This difference in performance is explained by the two distinct wear regimes. In the case of the 101-kW coating, a severe wear regime was observed, with a surface characterized by brittle fracture and subsequently grain pullout facilitated by poor inter-particle bonding, combined with regions of plastic deformation and a relatively erratic coefficient of friction. In the case of polycrystalline bulk alumina against alumina, a severe wear regime is expected only with sliding speeds above 0.1 m/s, or with a load above 100 N (Ref 20). In this case, a severe wear regime was produced at a speed of 0.01 m/s at 10 N. Coefficients of friction measured in the two 101-kW coating tests were initially high, up to 0.7 in both cases, followed by a rapid, slight decrease and then a gradual decrease toward 0.45. This is consistent with an initial adhesive wear mechanism associated with high contact pressure in which deformation of asperities and subsequent energy dissipation are reflected in increased frictional force. An adhesive mechanism at the initial stages of the wear process is consistent with other studies that explain the wear of a range of plasma-sprayed ceramic coatings (Ref 21). It is also known that initial wear mechanisms can begin as adhesive, in which generated wear particles are adhered or trapped, resulting in three-body abrasive wear, whereby trapped or joined debris also contributes to the abrasive wear process (Ref 22). Bolelli et al. (Ref 23) explained that for an alumina plasma-sprayed coating against an alumina counterbody, some coating material adhered to the counterbody; however, the main mechanism of wear was an abrasive mechanism involving brittle fracture. The higher micro-hardness and stiffness of the coating also relate to the brittle nature of 101-kW coatings. When we consider the difference in average fracture toughness of the two coatings, it is clear that the reduced fracture toughness of the 101-kW coating ( $0.5\text{--}2 \text{ MPa m}^{1/2}$ ) compared to  $2\text{--}5.5 \text{ MPa m}^{1/2}$  for the 72-kW coating) likely contributed to the severe wear regime which took place for the remainder of the wear test, since it is known that fracture toughness is a critical property for wear resistance against brittle fracture (Ref 20, 24). Inter-granular/inter-particle fracture followed by grain pullout hence explains the wear mechanism observed in the case of the 101-kW coating. The lower fracture toughness of the 101-kW coating also may have contributed to the higher friction observed compared to the 72-kW coating, given fracture toughness of ceramics is known to be an important property in their friction, with energy dissipated during fracture contributing to friction (Ref 25). Based on a range of ceramics including alumina, at a fracture toughness of  $1 \text{ MPa m}^{1/2}$ , coefficient of friction has been measured in excess of 0.8 against a diamond counterbody (Ref 25). This explains the high friction at the beginning of the wear test for the 101-kW coating. The rapid decrease in friction after the initial

rise to  $\sim 0.7$  is consistent with removal of the coating, and then the following gradual decrease in friction may be caused by formation of a film on the counterbody and/or the coating wear track created by the reattachment of wear debris. Tribofilm formation in atmospheric plasma spraying and HVOF alumina coatings was also reported by Bolelli et al. in the dry sliding wear of alumina coatings against alumina counterbodies (Ref 4, 23).

The 72-kW coating in contrast yielded a mild wear regime, with smooth surfaces on both coating and counterbody typical of plastic flow along with a smoother friction curve. In this case, the trend of coefficient of friction is quite opposite to that of the 101-kW coating. Here, coefficient of friction gradually increased to 0.4–0.45 consistent with the gradually increasing area of contact between surfaces. A lower friction value can be explained by the greater fracture toughness along with prevalence of harder alpha particles present in the coating providing a hard facing surface. The friction data in this case is also less erratic, indicative of a regime not involving brittle fracture/grain pullout, in contrast to the regime of the 101-kW coating.

In light of the nanoindentation data, it is clear that for both coating types, the material is comprised of harder phases in a matrix of a softer phase as seen with different color contrast in SEM and SPM images of Fig. 3 and 7, respectively. Based on XRD data analysis, for both samples, an amorphous phase dominated the coatings based on weight %. The hardness of amorphous alumina has previously been measured using nanoindentation in thin films with thickness less than  $1 \mu\text{m}$  (Ref 26), reporting a hardness between 5 and 8 GPa, in comparison with a crystalline form which was 11–12 GPa. In the referenced work, crystalline phases were characterized as containing the  $\gamma$ ,  $\delta$  and  $\theta$  forms of alumina. Amorphous thin film alumina has also been measured at  $<12 \text{ GPa}$ , in comparison with the crystalline alpha, measured between 18 and 21 GPa (Ref 27). In other work, amorphous alumina nanohardness was measured at a mean of between 12.5 and 13 GPa, with a range of approximately  $\pm 1 \text{ GPa}$ . Elastic modulus was also measured between 175 and 180 GPa (Ref 28), which fits the values of the matrix moduli for the coating matrices in Table 2 when considering the error ranges. In the present study, hardness of the “dark” color matrix for both coating types was measured between 3 and 14 GPa, with a mean of 11 and 9 GPa for the 101 and 72-kW samples, respectively. It is likely that the “dark” matrix in both coatings is predominantly comprised of amorphous alumina, with some regions of the respective crystalline phases present in each coating. Despite the maximum hardness of the non-matrix, alpha particle regions of the coating being notably higher,  $\sim 30 \text{ GPa}$ , the mean hardness of the coatings is not significantly different.

Therefore, the increased fracture toughness of the coatings caused by the prevalence of the tougher alpha phase is likely a greater contributor to the dry sliding wear resistance of SHVOF alumina coatings, as opposed to the hardness of the alpha particles themselves. This is particularly interesting given the clearly greater presence of



porosity and lower microhardness in the 72-kW coating, which is thought to worsen the fracture toughness of HVOF-sprayed ceramic coatings (Ref 29). In the case of fracture toughness measurements for both coating types, crack growth direction was solely interlamellar, i.e. between and parallel to the lamellae associated with splat formation, parallel to the coating surface. In the case of the 72-kW coating, despite the presence of the amorphous phase and porosity, crack growth was inhibited by the presence of alpha alumina relatively homogeneously distributed throughout the coating.

## 5. Conclusions

Two coatings of alumina were sprayed onto carbon steel substrates using two parameter settings using suspension HVOF. At combustion flame powers of 101 and 72 kW, based on Rietveld analysis, both coatings contained a majority of amorphous phase based on weight %. For the 101-kW processed coating, 26 wt.% of the coating was crystalline, of which ~95 wt.% was the less desirable gamma form of alumina and ~3 wt.% was the original alpha form. For the coating produced using 72-kW flame power, a higher level of crystallinity was measured, at ~42 wt.%, of which ~73 wt.% was alpha and ~26 wt.% gamma alumina. Hence by selection of processing parameters, a useful amount of original alpha alumina can be retained in the coating. The trade-off is that the porosity level was also increased in the 72-kW coating, and the coating had a lower microhardness of  $H_{10gf} = 11.7$  GPa and elastic modulus of  $E_{72kW} = 133$  GPa.

In ball-on-flat dry sliding wear against an alpha alumina counterbody, the 72-kW coating yielded a specific wear rate two orders of magnitude lower than the 101-kW coating, at  $4 \times 10^{-7}$  compared to  $2-4 \times 10^{-5}$  mm<sup>3</sup>/Nm, respectively.

The amorphous/gamma dominated 101-kW coating engaged in an initially very high friction regime despite the polished initial surface, with a COF up to 0.7 and gradually reducing to 0.4, consistent with an initial adhesive wear mechanism followed by an abrasive brittle fracture/grain pullout regime. The 72-kW coating in contrast underwent a mild wear regime under the same conditions, with only a smooth wear track produced characteristic of plastic flow. Mean fracture toughness of the 72-kW coating, measured via cross-sectional Vickers indentation, was approximately three times higher than that of the 101-kW coating, and hence the brittle fracture mechanism by which the 101-kW coating was worn was avoided via improved fracture toughness associated with the prevalence and good distribution of alpha particles. Hardness of the more prevalent alpha alumina in the 72-kW coatings may also have contributed to greater wear resistance.

## References

1. A. Killinger, M. Kuhn, and R. Gadow, High-Velocity Suspension Flame Spraying (HVSFS), a New Approach for Spraying

- Nanoparticles with Hypersonic Speed, *Surf. Coat. Technol.*, 2006, **201**(5), p 1922-1929
2. F.-L. Toma, L.-M. Berger, C.C. Stahr, T. Naumann, and S. Langner, Microstructures and Functional Properties of Suspension-Sprayed Al<sub>2</sub>O<sub>3</sub> and TiO<sub>2</sub> Coatings: An Overview, *J. Therm. Spray Technol.*, 2010, **19**(1), p 262-274
3. L. Pawlowski, *Thermal Spraying Techniques, the Science and Engineering of Thermal Spray Coatings*, Wiley, London, 2008, p 67-113
4. G. Bolelli, J. Rauch, V. Cannillo, A. Killinger, L. Lusvarghi, and R. Gadow, Microstructural and Tribological Investigation of High-Velocity Suspension Flame Sprayed (HVSFS) Al<sub>2</sub>O<sub>3</sub> Coatings, *J. Therm. Spray Technol.*, 2008, **18**(1), p 35-49
5. R. McPherson, Formation of Metastable Phases in Flame- and Plasma-Prepared Alumina, *J. Mater. Sci.*, 1973, **8**(6), p 851-858
6. P. Fauchais, G. Montavon, and G. Bertrand, From Powders to Thermally Sprayed Coatings, *J. Therm. Spray Technol.*, 2010, **19**(1), p 56-80
7. R. McPherson, On the Formation of Thermally Sprayed Alumina Coatings, *J. Mater. Sci.*, 1980, **15**(12), p 3141-3149
8. P. Chráska, J. Dubsy, K. Neufuss, and J. Písacka, Alumina-Base Plasma-Sprayed Materials Part I: Phase Stability of Alumina and Alumina-Chromia, *J. Therm. Spray Technol.*, 1997, **6**(3), p 320-326
9. J. Ilavsky, C.C. Berndt, H. Herman, P. Chraska, and J. Dubsy, Alumina-Base Plasma-Sprayed Materials—Part II: Phase Transformations in Aluminas, *J. Therm. Spray Technol.*, 1997, **6**(4), p 439-444
10. F.-L. Toma, L.-M. Berger, S. Scheitz, S. Langner, C. Rödel, A. Potthoff, V. Sauchuk, and M. Kusnezoff, Comparison of the Microstructural Characteristics and Electrical Properties of Thermally Sprayed Al<sub>2</sub>O<sub>3</sub> Coatings from Aqueous Suspensions and Feedstock Powders, *J. Therm. Spray Technol.*, 2012, **21**(3), p 480-488
11. J. Rauch, G. Bolelli, A. Killinger, R. Gadow, V. Cannillo, and L. Lusvarghi, Advances in High Velocity Suspension Flame Spraying (HVSFS), *Surf. Coat. Technol.*, 2009, **203**(15), p 2131-2138
12. H. Rietveld, Line Profiles of Neutron Powder-Diffraction Peaks for Structure Refinement, *Acta Crystallogr. A*, 1967, **22**(1), p 151-152
13. J. Suffner, H. Sieger, H. Hahn, S. Dosta, I.G. Cano, J.M. Guilemany, P. Klimczyk, and L. Jaworska, Microstructure and Mechanical Properties of Near-Eutectic ZrO<sub>2</sub>-60 wt% Al<sub>2</sub>O<sub>3</sub> Produced by Quenched Plasma Spraying, *Mater. Sci. Eng., A*, 2009, **506**(1-2), p 180-186
14. R.S. Zhou and R.L. Snyder, Structures and Transformation Mechanisms of the  $\eta$ ,  $\gamma$  and  $\theta$  Transition Aluminas, *Acta Crystallogr. Sect. B*, 1991, **47**(5), p 617-630
15. W.C. Oliver and G.M. Pharr, An Improved Technique for Determining Hardness and Elastic Modulus Using Load and Displacement Sensing Indentation Experiments, *J. Mater. Res.*, 1992, **7**(06), p 1564-1583
16. A.G. Evans and E.A. Charles, Fracture Toughness Determinations by Indentation, *J. Am. Ceram. Soc.*, 1976, **59**(7-8), p 371-372
17. B. Yazdani, F. Xu, I. Ahmad, X. Hou, Y. Xia, and Y. Zhu, Tribological Performance of Graphene/Carbon Nanotube Hybrid Reinforced Al<sub>2</sub>O<sub>3</sub> Composites, *Sci. Rep.*, 2015, **5**, p 11579
18. T. Hussain, E.C. Shaw, Z. Pala, F. Xu, A.S.M. Ang, Tribology and Nanoindentation Study of Suspension HVOF Thermally Sprayed Alumina Coating, *International Thermal Spray Conference & Exposition*, May 10-12, 2016 (Shanghai, China)
19. J. Gangwar, K. Dey, P. Komal, S. Tripathi, and A. Srivastava, Microstructure, Phase Formations and Optical Bands in Nanostructured Alumina, *Adv. Mater. Lett.*, 2011, **2**, p 402-408
20. I.M. Hutchings, *Tribology: Friction and Wear of Engineering Materials*, Edward Arnold, London, 1992
21. Y. Jin and Y. Yang, Tribological Behavior of Various Plasma-Sprayed Ceramic Coatings, *Surf. Coat. Technol.*, 1997, **88**(1), p 248-254
22. B. Bhushan, *Introduction to Tribology*, Wiley, New York, 2002

23. G. Bolelli, V. Cannillo, L. Lusvarghi, and T. Manfredini, Wear Behaviour of Thermally Sprayed Ceramic Oxide Coatings, *Wear*, 2006, **261**(11-12), p 1298-1315
24. R. Singha Roy, A. Mondal, A. Chanda, D. Basu, and M.K. Mitra, Sliding Wear Behavior of Submicron-Grained Alumina in Biological Environment, *J. Biomed. Mater. Res., Part A*, 2007, **83A**(2), p 257-262
25. H. Ishigaki, I. Kawaguchi, M. Iwasa, and Y. Toibana, Friction and Wear of Hot Pressed Silicon Nitride and Other Ceramics, *J. Tribol.*, 1986, **108**(4), p 514-521
26. P. Nayar, A. Khanna, D. Kabiraj, S.R. Abhilash, B.D. Beake, Y. Losset, and B. Chen, Structural, Optical and Mechanical Properties of Amorphous and Crystalline Alumina Thin Films, *Thin Solid Films*, 2014, **568**, p 19-24
27. Q. Li, Y.-H. Yu, C. Singh Bhatia, L.D. Marks, S.C. Lee, and Y.W. Chung, Low-Temperature Magnetron Sputter-Deposition, Hardness, and Electrical Resistivity of Amorphous and Crystalline Alumina Thin Films, *J. Vac. Sci. Technol., A*, 2000, **18**(5), p 2333-2338
28. P.M. Martin, *Thin Film Tribological Materials. Introduction to Surface Engineering and Functionally Engineered Materials*, Wiley, New York, 2011, p 187-282
29. L. Pawlowski, *The Science and Engineering of Thermal Spray Coatings*, Wiley, New York, 1995